THE DYNAMICAL INFLUENCE OF A PLANET AT SEMIMAJOR AXIS 3.4 AU ON THE DUST AROUND ε ERIDANI

SEAN M. MORAN

Astronomy Department, California Institute of Technology, MC 105-24, Pasadena, CA 91125; smm@astro.caltech.edu

MARC J. KUCHNER[1]

Department of Astrophysical Sciences, Princeton University, Peyton Hall, Princeton, NJ 08544; mkuchner@astro.princeton.edu

AND

MATTHEW J. HOLMAN

Harvard-Smithsonian Center for Astrophysics, 60 Garden Street, Cambridge, MA 02138; mholman@cfa.harvard.edu

ABSTRACT

Precise Doppler experiments suggest that a massive ($m \sin i = 0.86 M_J$) planet orbits at semimajor axis $a = 3.4$ AU around ε Eri, a nearby star with a massive debris disk. The dynamical perturbations from such a planet would mold the distribution of dust around this star. We numerically integrated the orbits of dust grains in this system to predict the central dust-cloud structure. For a supply of grains that begin in low-inclination, low-eccentricity orbits at 15 AU, the primary feature of the dust distribution is a pair of dense clumps containing dust particles trapped in mean-motion resonances of the form n:1. These clumps appear to revolve around the star once every two planet revolutions. Future observations with the IRAM Plateau de Bure Interferometer, the Submillimeter Array (SMA), or the Atacama Large Millimeter Array (ALMA) could detect these clumps, confirming the existence of the planet and revealing its location.

Subject headings: celestial mechanics — circumstellar matter — interplanetary medium — planetary systems — stars: individual (ε Eri)

1. INTRODUCTION

Some nearby main-sequence stars appear to host debris belts like the asteroid belt and the Kuiper Belt in our solar system; see the reviews by Backman & Paresce (1993) and Zuckerman (2001). Extrasolar asteroids and Kuiper Belt objects can reveal themselves by generating clouds of circumstellar dust that emit thermally in excess of the stellar photospheric emission. The *Infrared Astronomical Satellite* (*IRAS*) discovered dozens of Vega-like stars that show signs of circumstellar dust, and upcoming observatories such as the Keck Interferometer, the *Spitzer Space Telescope*, the *James Webb Space Telescope* (*JWST*), and the *Darwin* Terrestrial Planet Finder (TPF) should detect many more.

The small-body belts in our solar system bear the dynamical signatures of planets; perhaps their extrasolar analogs do too. Millimeter and submillimeter images of dust rings around Vega and the Vega-like stars β Pic, Fomalhaut, and ε Eri all show clumps and asymmetries (Holland et al. 1998; Greaves et al. 1998; Koerner et al. 2001; Wilner et al. 2002; Holland et al. 2003). Dust spiraling past a planet under the influence of Poynting-Robertson (P-R) drag (Robertson 1937; Wyatt & Whipple 1950) can become temporarily trapped in exterior mean-motion resonances (MMRs) with the planet, forming rings of enhanced dust density (Gold 1975) like the one created by Earth in the solar zodiacal cloud (Dermott et al. 1994; Reach et al. 1995). Locating clumps and holes in these rings can constrain the position, mass, and orbital eccentricity of the perturbing planet (Kuchner & Holman 2003; Kuchner 2003).

Of the four Vega-like stars mentioned above, the K2 V star ε Eri is closest to Earth at a distance of 3.22 pc. Greaves et al.

(1998) imaged a blobby ring of emission around ε Eri at 850 μm using the Submillimeter Common-User Bolometric Array (SCUBA) on the James Clerk Maxwell Telescope (JCMT). Quillen & Thorndike (2002) have modeled the blobs in this ring and suggest that a perturbing planet at a semimajor axis of ∼40 AU could be responsible for the observed asymmetries. One might consider this ring at ∼60 AU to be an analog of the Kuiper Belt, perturbed by Neptune (Liou & Zook 1999; Moro-Martín & Malhotra 2003), although the ε Eri Neptune analog has an eccentric orbit.

The ε Eri system may also contain a circumstellar emission peak within a few arcseconds (<20 AU) of the star (Beichman et al. 1988; Greaves et al. 1998; Dent et al. 2000; Li et al. 2003), and probably a second planet. Precise Doppler measurements suggest that a massive planet ($m \sin i = 0.86 \pm 0.05 M_J$) orbits ε Eri in an eccentric orbit ($e = 0.6 \pm 0.2$) at semimajor axis $a = 3.4 \pm 0.1$ AU (Campbell et al. 1988; Cumming et al. 1999; Hatzes et al. 2000). Interpretation of these data remains controversial, partially because of the fact that ε Eri is young and active (Gray & Baliunas 1995), despite a preliminary astrometric detection of the planet (Gatewood 2000).

The dust responsible for the emission inside ∼20 AU would eventually spiral past this precise-Doppler planet, which could easily trap dust temporarily in MMRs. Present images can barely resolve the disk interior to 20 AU, but future high-resolution observations could probe this region of the debris disk and investigate the cloud structure created by the planet. ε Eri's inner dust cloud may resemble the solar zodiacal cloud perturbed by planets of the inner solar system, although the inner ε Eri planet has an eccentric orbit.

Li et al. (2003) have questioned the existence of the central submillimeter emission peak, suggesting that it may be due to

noise. Initial images taken by the *Spitzer Space Telescope*[2] of another debris-disk system, Fomalhaut, reveal mid-IR emission from warm dust occupying a central region of the system that had appeared relatively empty in earlier submillimeter images (Holland et al. 1998). In addition, the excess flux detected by *IRAS* at 25 μm around ϵ Eri was contained in a beam sensitive only to the inner 20 AU of the system (Beichman et al. 1988). Even if the claimed central submillimeter emission is spurious, it is still likely that ϵ Eri contains a central dust cloud; if the radial velocity planet is real, this cloud should reflect its presence.

The ϵ Eri system provides a rare opportunity to compare dust-cloud simulations to images of a nearby, roughly face-on debris disk, in a case in which some orbital parameters of the perturbing planet are independently measurable, to build a bridge between different dynamical methods for detecting extrasolar planets. In this paper, we examine the inner "exozodiacal" component of the ϵ Eri dust near the precise-Doppler planet. We use numerical simulations of the interaction of a planet and a dust cloud to predict what observations might reveal at $\leq$20 AU in this system. We consider how dust-cloud imaging could test the existence of the reported planet and, if it exists, constrain its properties.

2. SIMULATION PARAMETERS

To model the effect of the precise-Doppler planet on the dust around ϵ Eri, we numerically integrated the equations of motion for dust grains (Liou & Zook 1999) using a symplectic *n*-body map (Wisdom & Holman 1991) modified to include terms for radiation pressure and P-R drag (Wilner et al. 2002). We did not attempt to model the effect of collisions on the eventual distribution of dust. In each simulation, we integrated the orbits of 1000 dust grains for a maximum of 5×10^8 yr, the approximate age of the ϵ Eri system. We stopped integrating a particle's orbit if it entered the planet's Hill sphere or reached an orbit with eccentricity $e_{\rm dust} > 1.0$ or semimajor axis $a_{\rm dust} > 200$ AU or $a_{\rm dust} < 0.1$ AU.

2.1. *The Planet*

Hatzes et al. (2000) combined radial velocity data from several sources (McDonald Observatory, Lick Observatory, the European Southern Observatory at La Silla, and the Canada-France-Hawaii Telescope) and deduced that the planet's orbit has semimajor axis $a = 3.4 \pm 0.05$ AU and eccentricity $e = 0.6 \pm 0.05$. Radial velocity data from Lick Observatory[3] considered alone yield a different eccentricity ($e = 0.43$), suggesting that the true uncertainties in the planet's orbital parameters are quite high. We show simulations with $e = 0.6$, although we tried simulations with both values and found no significant difference in the cloud morphology.

Our dynamical models probe the full three-dimensional structure of the dust cloud. They require as input the inclination, i, and the longitude of ascending node, Ω, of the planet, orbital elements unconstrained by radial velocity measurements. For the purposes of this exploration, we used i and Ω from preliminary astrometric work by Gatewood (2000). Our models will ultimately test the astrometric measurements.

We assume that the inclination of the planet's orbit to the line of sight is $i = 46°$, which Gatewood (2000) determined to

be the best fit to astrometric and radial velocity data. The Gatewood (2000) value has a large uncertainty ($\pm17°$), so it is roughly consistent with values suggested by the shape of the outer ring of 850 μm emission (Greaves et al. 1998) and the tilt of the stellar pole (Saar & Osten 1997). The amplitude of the radial velocity variations constrains the mass of the planet to $m \sin i = 0.86 \pm 0.05 M_{\rm J}$ (Hatzes et al. 2000), given the mass of the star ($M_* = 0.8\ M_\odot$). For $i = 46°$, this gives $m = 1.20 M_{\rm J}$. We discuss the effects of varying planet mass and inclination in § 4. We adopt a longitude of ascending node of $\Omega = 120°$ (Gatewood 2000) and an argument of pericenter of $\varpi = 49°$ (Hatzes et al. 2000). These parameters are only weakly constrained by data, but variations affect only the observed orientation of any dust-cloud structure.

2.2. *The Dust Grains*

Recent models (Sheret et al. 2004; Li et al. 2003; Dent et al. 2000) attempt to use the ϵ Eri spectral energy distribution and the azimuthally averaged radial profile from the 850 μm image to constrain dust-grain properties. However, the grains in the center of the cloud may not resemble the grains in the outer ring; they are likely to be smaller and more collisionally processed. We adopt a dust-grain size of $s = 15\ \mu$m for all of our simulations, a typical grain size for the solar zodiacal cloud. We discuss the effects of varying grain size in § 4.

For spherical grains, the radiation pressure factor, β, which determines the strength of the P-R force, is related to the grain size by $\beta = 3L_*/(16\pi c G M_* \rho s)$, where s is the grain radius in microns and ρ is the dust-grain density (Wyatt & Whipple 1950; Burns 1976). Assuming $\rho = 2$ g cm^{-3} gives $\beta = (0.099\ \mu$m$)/s$ for grains orbiting ϵ Eri. For 15 μm grains, this corresponds to $\beta = 0.007$.

In order to generate snapshots of the dust distribution at several different phases of the planet, we use a procedure nearly identical to that used by Wilner et al. (2002) to create face-on disk models. Kuchner & Holman (2001) used a similar procedure to schematically illustrate disk structures. Quillen & Thorndike (2002) also created disk models in this fashion but restricted their simulations to two dimensions. We record the position of each particle throughout the integration at regular intervals corresponding to four particular phases of the planet's orbit, rotating the three-dimensional positions into a coordinate system tilted 46° from face-on. Then we sort these positions into four three-dimensional histograms that model the density distribution of dust in an inertial frame at each of the four orbital phases, assuming a steady-state source.

We calculate the emission from the density distribution using ZODIPIC[4] (Kuchner & Serabyn 2002; Danchi et al. 2003), assuming the cloud is optically thin, and we scale the column density so the total 25 μm flux matches that measured by *IRAS*. As mentioned above, at this wavelength *IRAS* was sensitive to emission within approximately 20 AU of ϵ Eri, the size of our simulated images.

ZODIPIC iteratively calculates dust-grain temperatures for grains in equilibrium with stellar radiation. We model the photospheric emission from the star by a blackbody at 5156 K (Bell & Gustafsson 1989), with luminosity $L_* = 0.34\ L_\odot$ and distance 3.218 pc. We assume a simple modified blackbody model for dust-grain emission. At wavelengths longer than some critical wavelength, λ_0, a dust grain's emission coefficient, ϵ, decreases roughly according to a power law $\epsilon =$
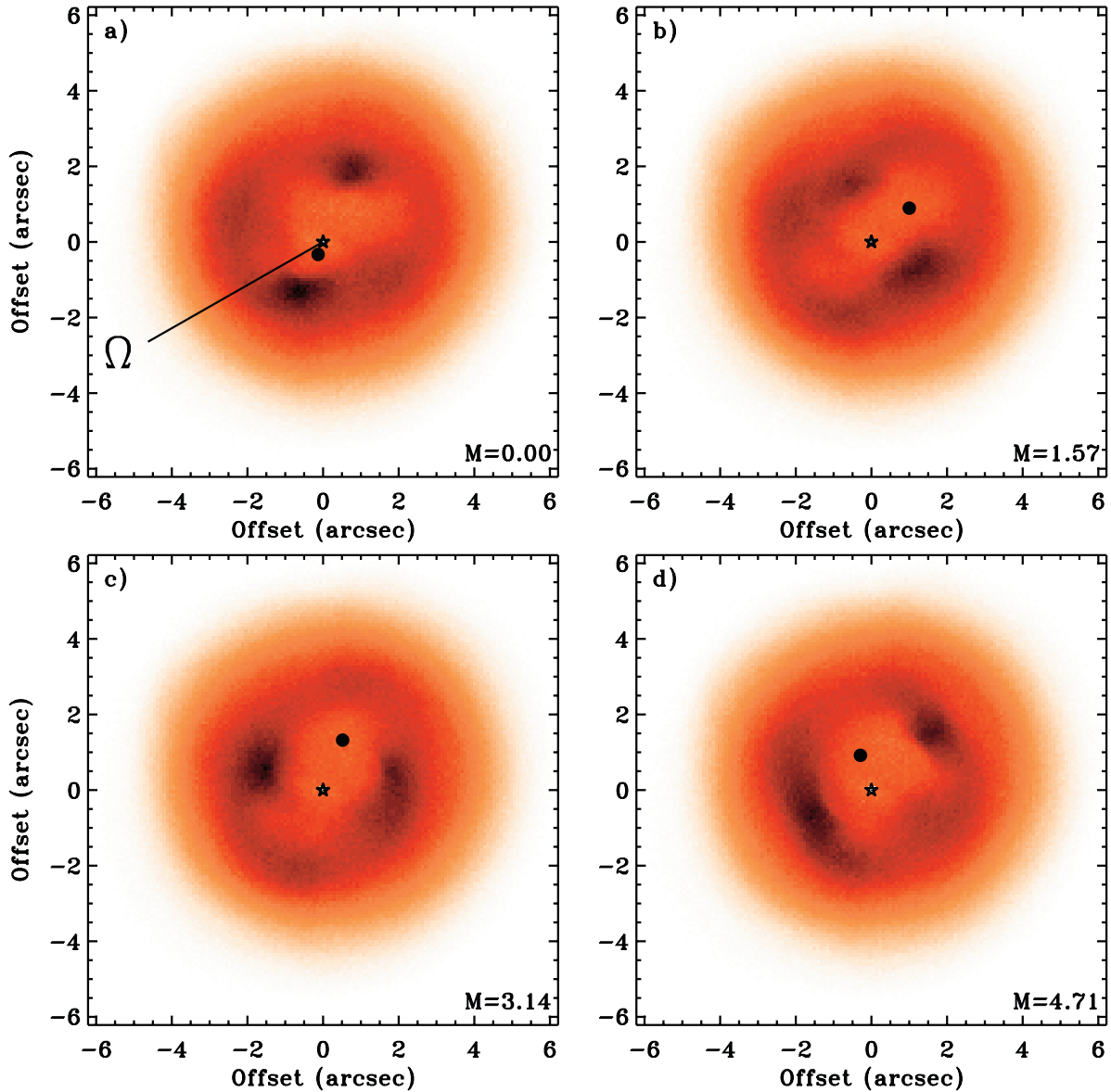

Fig. 1.—Simulated dust distribution for source grains beginning on low-eccentricity orbits. The snapshots show the structure at four different orbital phases of the planet: (a) $M = 0$, (b) $M = \pi/2$, (c) $M = \pi$, and (d) $M = 3\pi/2$. A filled circle represents the planet, and a star symbol denotes the star.

$\epsilon_0 (\lambda_0/\lambda)^q$. At wavelengths shorter than λ_0, we hold ϵ constant. We assume amorphous, moderately absorbing grains for which $q = 1.0$ and λ_0 equals the grain radius (Backman & Paresce 1993). This choice falls between the porous grains favored by Li et al. (2003) and the more solid grains favored by Sheret et al. (2004). We discuss the uncertainty in dust emission properties in § 4.

The initial particle inclinations i' were chosen from a uniform distribution on the interval $[0°, 5°]$, where $i' = 0°$ corresponds to the plane of the planet's orbit. The initial ascending node, argument of periapse, and mean anomaly for each particle were selected from a uniform distribution on the interval $[0, 2\pi)$. We explored a range of initial particle eccentricities.

3. SIMULATION RESULTS

Since the P-R timescale for dust around ε Eri is less than the age of the system, none of the observed dust can be considered primordial; its presence requires the existence of dust-generating bodies in the system. We present the results of two simulations with different initial conditions, meant to model dust grains generated by different populations of small bodies. We choose to study two populations that have analogs in our solar system, one in which dust grains begin on low-eccentricity orbits and one in which they begin on highly eccentric orbits. Later in this section, we discuss the parameter space between these two extremes.

3.1. Asteroid-Dust Model

For the first model, we started the grains on orbits with semimajor axes $a = 15$ AU and eccentricities chosen from a uniform distribution on the interval $[0.05, 0.15]$. This model represents dust generated in a belt of small bodies on low-inclination orbits like the asteroid belt. Figure 1 shows four snapshots of the model at 850 μm, when the planet's mean anomaly is $M = 0$, $\pi/2$, π, and $3\pi/2$.

The results resemble the model for the Vega disk by Wilner et al. (2002). The primary observable structure the planet
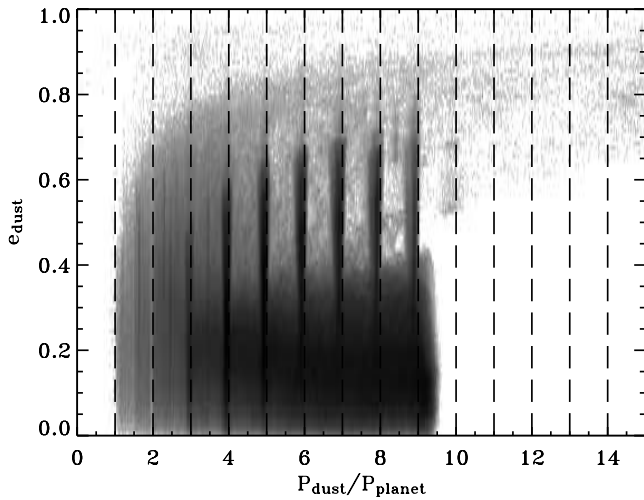
FIG. 2.—Histogram of relative dust concentration as a function of period and eccentricity for the model shown in Fig. 1. Dust concentration is displayed on a logarithmic scale.
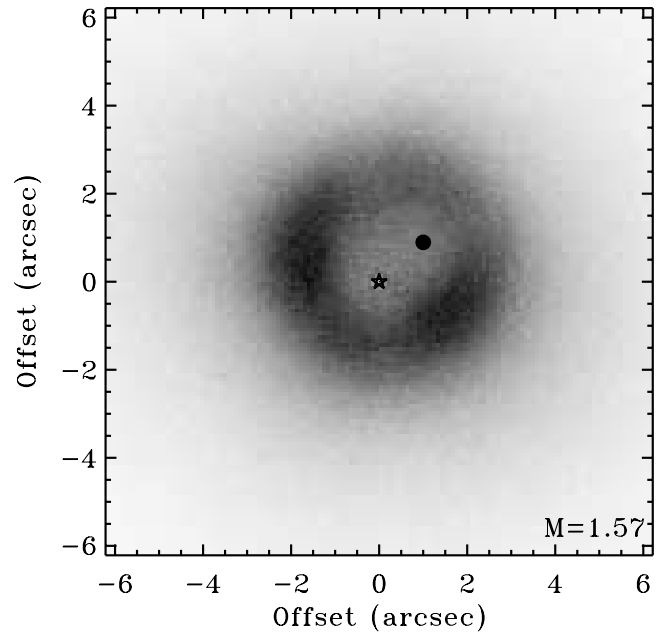

FIG. 3.—Simulated dust distribution for source grains beginning on high-eccentricity orbits with semimajor axes of 50 AU. The structure does not vary with the planet's orbital phase.

carves in the dust distribution is a pair of clumps that appears to orbit the star once for every two orbits of the planet. The clumps occupy circumstellar radii of roughly 5–10 AU. This zone corresponds roughly to the orbit of dust with $e_{dust} = 0.4$ in the 3:1 exterior MMR.

Figure 2 shows a histogram of the dust concentration as a function of eccentricity and orbital period for the particles represented in Figure 1. The dust was released at $a = 15$ AU, where the dust orbital period, P_{dust}, is approximately 9.3 times the orbital period of the planet, P_{planet}. In Figure 2, particles trapped in MMRs form dark vertical bars; the bars at $P_{dust}/P_{planet} = 3, 4, 5, \ldots, 9$ show that the resonantly trapped grains in this model primarily occupy the 3:1 through 9:1 exterior MMRs. Fainter dark lines are also visible at the periods of other resonances, notably the 5:2 and 7:2 exterior MMRs. Dust is captured most strongly into the 3:1 and 4:1 resonances.

Kuchner & Holman (2003) illustrated four principal structures a planet could create in an optically thin disk of dust released on low-eccentricity orbits. Our asteroid-dust model for ϵ Eri corresponds to case IV in that paper, the high-mass planet on a moderately eccentric orbit. The Quillen & Thorndike (2002) model of the outer ring corresponds to case III; ϵ Eri could host both a case III dust ring and a case IV dust ring. Figure 2 illustrates that the eccentricities of the dust grains in the MMRs range from zero to roughly the planet's eccentricity (0.6), as described in Kuchner & Holman (2003).

In addition to the dust clumps, Figure 1 shows a torus of dust particles that is not centered on the star. This torus appears to be generated at the same time as the clumps by the mechanism described in Kuchner & Holman (2003). Figure 2 reveals that most of the dust in nonresonant orbits is concentrated in orbits with $e_{dust} < 0.4$. But the offset of the center of the torus ($\sim0\farcs5$) from the star shows that it must contain higher eccentricity particles, such as those in the most distant n:1 MMRs.

To first order, changing the mass of the planet, the initial semimajor axis of the dust, or β only changes which resonances are populated; e.g., for more massive planets, more distant resonances dominate. However, for planets much more massive than Neptune, the dominant MMRs are always of the form n:1. Since MMRs of the form n:1 generally

produce a two-clump structure, the appearance of the cloud hardly changes whether MMRs 2:1–5:1 dominate or MMRs 5:1–8:1 dominate, for example. Consequently, the basic resonant pattern is robust to changes in the above-mentioned parameters.

3.2. Comet-Dust Model

We also considered dust released at higher orbital eccentricities. Such dust could be generated by small bodies in eccentric orbits, like comets in our solar system. The outer ring may scatter such objects inward just as the Kuiper Belt leaks comets into the inner solar system (Fernandez 1980; Duncan et al. 1988; Levison & Duncan 1997).

Figure 3 shows an extreme example: a 1000 particle model with initial dust semimajor axes $a_{dust} = 50$ AU and eccentricities chosen from a uniform distribution on the interval $[0.8, 0.9]$. The choice of semimajor axis is motivated by the location of the Kuiper Belt in the solar system. For such high eccentricities, however, moderate changes in initial semimajor axis will do little to alter a particle's steep initial approach to the center of the system.

This model generates a substantially different cloud morphology than the asteroid-dust model described above. This comet-dust model has a torus of emission but no resonant dust clumps. The inclination of the torus produces two limb-brightened areas where the optical depth through the torus is highest. These enhancements resemble the rotating clumps of Figure 1, but, unlike the clumps generated by dust in MMRs, the emission enhancements due to limb-brightening do not vary with time.

Figure 4 shows the histogram of dust concentration as a function of eccentricity and orbital period for the dust in Figure 3. This histogram lacks the dark vertical bars that appear in Figure 2 indicating dust trapped in the 3:1 through 9:1 MMRs. These regions of the histogram in Figure 4 are relatively unpopulated, suggesting that the dust released at high orbital eccentricities avoids these n:1 MMRs. Faint dark
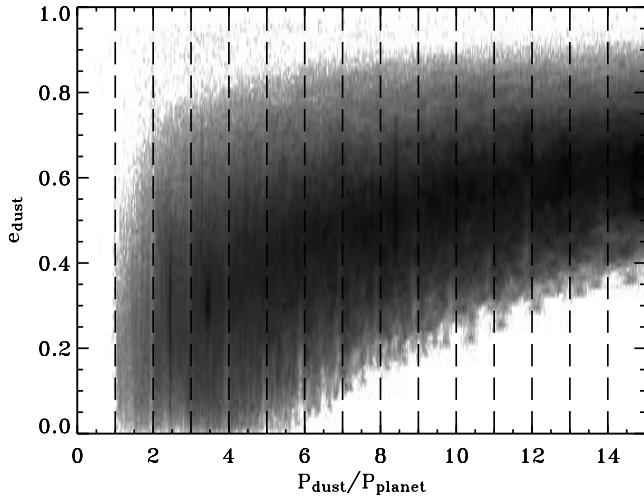
FIG. 4.—Histogram of relative dust concentration as a function of period and eccentricity for the comet-dust model shown in Fig. 3.

FIG. 5.—Azimuthally averaged radial profile of the ϵ Eri dust disk at 850 μm. The open diamonds with error bars are from Greaves et al. (1998). The solid line is the radial profile of our asteroid-dust model, convolved with a Gaussian of 15″ FWHM. The dashed line is the same for our comet-dust model. For clarity, we include the radial profile of a simple symmetric ring centered at 72 AU, consisting of grains with the same properties as our inner-ring dust models. Both asteroid and comet models are consistent with the inner-ring radial profile (<20 AU).

bars appear at the locations of several other MMRs, but they represent only weak enhancements over the background of particles in nonresonant orbits.

Because fewer comet-dust particles become trapped in MMRs, dust grains in the comet-dust simulation pass through the central 6″ more rapidly, on average, than grains in the asteroid-dust simulation described above. The mean lifetime of a dust grain in Figure 3 is $\tau \sim 5.5 \times 10^6$ yr, compared to $\tau \sim 8 \times 10^6$ yr for the dust in Figure 1. This shorter dust lifetime reduces the amount of information that goes into each snapshot of dust density. As a result, Figure 3 appears grainier than Figure 1.

The resonant dust clumps seen in Figure 1 seem to emerge only when the dust originates on low-eccentricity orbits. By running a set of brief simulations of 100 particles each, we traced the initial dust-grain eccentricity at which the resonant clumps begin to vanish. Dust grains released with eccentricities as high as 0.4 continue to be trapped in the n:1 MMRs, but the clumps become fainter and fainter as the initial e_{dust} is increased. At initial dust orbital eccentricities greater than $e_{dust} \approx 0.6$, our simulations no longer show any sign of trapping in the n:1 MMRs.

This critical eccentricity is the eccentricity of the planet's orbit. The disappearance of clumps may simply reflect when the orbits of particles in the key MMRs begin to intersect the orbit of the planet. Particles in the 3:1 exterior MMR would become planet-crossing at some longitudes of pericenter at an eccentricity of $e_{dust} \approx 0.2$. At $e_{dust} \approx 0.8$, all particles at the nominal semimajor axis of this resonance must cross the planet's orbit.

4. DISCUSSION

To match the observed total emission from dust in the central 6″ of the ϵ Eri cloud, our simulations require a mass of 0.1 lunar masses (~7×10^{24} g) of 15 μm dust grains. The mean line-of-sight optical depth for both asteroid- and comet-dust models is 5×10^{-3}. Both the resonant blobs of the asteroid-dust model and the limb-brightened regions of the comet-dust model have line-of-sight optical depths of approximately 0.02.

A better calculation of the dust mass in the system's center depends on a realistic model for dust-grain size distribution and physical characteristics (porosity, etc). Models similar to those
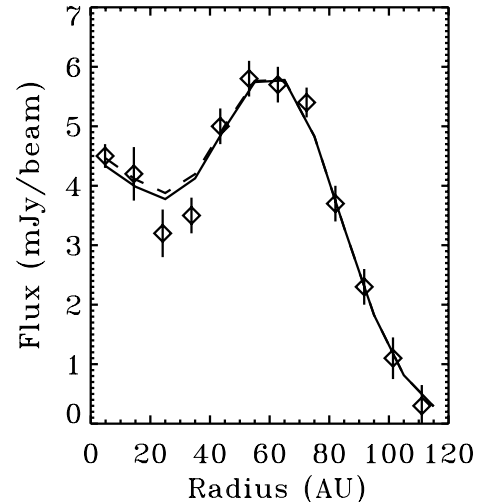
in Li et al. (2003) and Sheret et al. (2004) might give more accurate mass estimations, but because of the lack of observational constraints, none yet exist for the central zodiacal cloud of ϵ Eri. Regardless of the physical model used to calculate dust mass, most of the mass in the debris disk will reside in the source population of small bodies.

Our simulated dust clouds are nevertheless consistent with current observations of the inner dust cloud for both the asteroid and comet models. Based on the dust-grain physical properties and emission characteristics discussed in § 2.2, we generate 850 μm, azimuthally averaged, radial profiles of our simulated dust clouds. These are convolved with a Gaussian of full width half-maximum (FWHM) 15″ to match the resolution of the Greaves et al. (1998) image. Figure 5 presents these radial profiles plotted against the Greaves et al. (1998) radial profile. Both models are consistent with the observed profile. In addition, the total 850 μm flux within 20 AU implies a total flux at 25 μm that is consistent with the 25 μm IRAS excess (Beichman et al. 1988).

When the planet mass is varied by $\pm 0.4 M_J$, a range consistent with current uncertainties in inclination and $m \sin i$, as well as the uncertainty in the mass determination of Gatewood (2000), we find no significant difference in the cloud morphology. Aside from its effect on planet mass, varying the inclination of the planet's orbit would affect only the projected separation between any dust blobs (or rings) and the central star. However, only in the extreme case of a nearly edge-on planetary orbit would the observed dust morphology be unrecognizable; since all observations of ϵ Eri indicate a roughly face-on orientation, we do not believe that inclination effects are a serious concern.

4.1. *Shortcomings of the Models*

A weakness of our simulations is that we cannot properly account for collisions between grains. The timescale for dust-grain collisions within the inner ring of dust ($\tau_\perp = 1.0 \times 10^{-4}$) is long compared to collision timescales in the debris disks
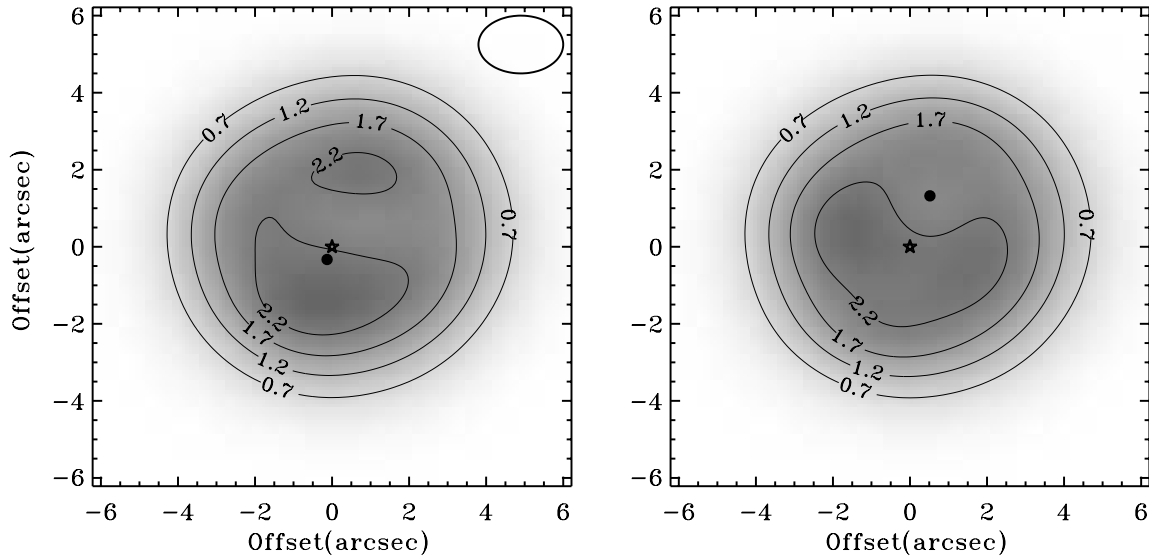
FIG. 6.—Simulated observations of the asteroid-dust model at two different phases of the planet's orbit, as seen by the IRAM PdBI at 1.3 mm. Contours indicate the surface brightness in mJy beam^{-1}. The locations of the blobs reflect the planet's argument of pericenter (49°).

around Vega, β Pic, and Fomalhaut (Dent et al. 2000), but still less than 10^5 yr for grains within 20 AU of the star, shorter than the P-R timescale (10^6–10^7 yr). In the absence of larger bodies, collisions tend to limit the maximum dust density in any given area by destroying grains. On the other hand, grains colliding with larger bodies can generate dust. The short collisional lifetime of the grains suggests that the dust may be generated by bodies closer to the star than the 15 AU asteroid belt we simulated—bodies that are perhaps themselves in resonant orbits with the planet.

Our simulations were performed with dust grains having a uniform value of β, a consequence of adopting a uniform dust-grain size. In general, increasing β, or equivalently decreasing the grain size, increases the sharpness of features in our dust images. The reverse is true when β is decreased (or grain size is increased). A more physically realistic simulation would include a range of dust-grain sizes; because the sharpness of features depends on β, we expect actual observations to reveal features that are somewhat less sharp than the ones presented here.

The precise-Doppler planet would interact secularly with the planet predicted by Quillen & Thorndike (2002) on a timescale of 10^8–10^9 yr. The structure of the outer ring, with its longer P-R time, may reflect this interaction, although the secular perturbations of the outer planet on the inner planet and inner dust ring probably have little consequence. However, the system could contain other unknown planets, which could add significant perturbations.

4.2. Future Observations

Observations of the inner regions of ϵ Eri with future telescopes might allow us to not only confirm the existence of the planet but also infer the existence of an asteroid belt or some other source of dust located within the outer dust ring. To assess the detectability of the expected dust morphology, we convolved our simulated images with Gaussians representing the beams of several current and planned telescopes. Figure 6 presents convolved images of the dust structure at two different phases of the planet, as the IRAM Plateau de Bure Interferometer (PdBI) might see them at 1.3 mm. We simulate

an elliptical beam for the PdBI, $1\farcs5 \times 2\farcs2$ FWHM, appropriate for a source at the declination of ϵ Eri, observed by the PdBI in the CD configuration. Figure 7 shows similar images for the Submillimeter Array (SMA) at 450 μm. In each image, we remove 90% of the starlight before convolution.

Observations with the PdBI at 1.3 mm may marginally resolve the dust blobs. The expected emission at 1.3 mm, based on the IRAS photometry, is very close to the sensitivity limit of the PdBI (0.7 mJy beam^{-1}). At this level, the probability of detection depends critically on the physical model used to predict dust emission at 1.3 mm from the observed 25 μm flux. Deviations from our modified blackbody emission model could reduce the expected flux to a level below the detection threshold or enhance it to provide a higher confidence detection.

Observations with the SMA at 450 μm should provide higher angular resolution, although the expected flux levels will remain close to the detection limit ($\sim$8 mJy beam^{-1}). We expect the SMA to easily separate the dust emission from the stellar emission, although it may still be difficult to simultaneously achieve the sensitivity and resolution needed to resolve individual dust clumps. In general, an instrument must achieve a resolution of better than $\sim3''$ in order resolve the dust blobs.

Although *Spitzer* is scheduled make observations of the ϵ Eri circumstellar disk, the proximity of our dust blobs to the central star will make it difficult to separate them from the stellar glare. At wave bands at which *Spitzer* may achieve the necessary $3''$ resolution, the photospheric emission from the star will most likely obscure any faint emission from the dust.

Figures 8 and 9 show simulated images of our comet-dust model, as seen by the PdBI and the SMA, respectively. These simulated images show that a single detection of dust blobs in ϵ Eri would be ambiguous. Multiple observations spanning a few years are required to test whether or not the dust blobs move. Detecting revolving clumps would support the asteroid-dust model, confirming the existence of the planet and constraining its ascending node, inclination, and longitude of pericenter.

Yet even if the revolving clumps are not found, we may still be able to use the cloud morphology to confirm the existence
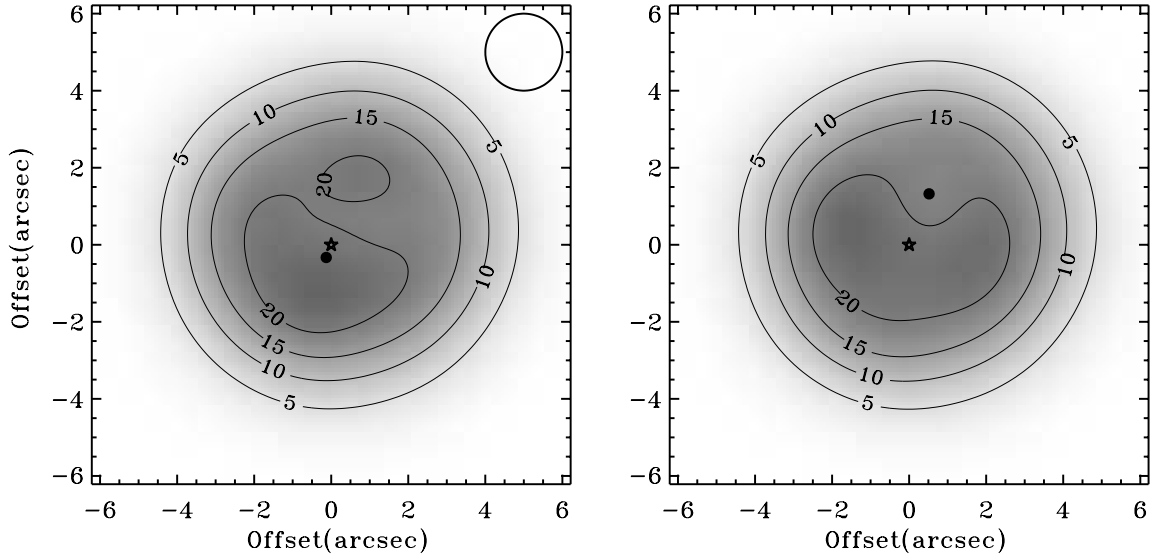
Fig. 7.—Simulated observations of the asteroid-dust model as seen by the SMA at 450 μm. Contours indicate the surface brightness in mJy beam^{-1}.

of the planet. As Figure 3 shows, the torus of dust that develops when we have eccentric particles has an inner void that is approximately circular, but the circle is not centered on the star. Detecting that the inner cutoff of the dust cloud is a circle not centered on the star would also be a sign of planetary perturbations, and it would constrain the planet's ascending node, inclination, and longitude of pericenter.

The Atacama Large Millimeter Array (ALMA) should provide greatly enhanced sensitivity along with spatial resolution equal to that of the simulated images in Figures 1 and 3. This array should easily resolve any dust structure created by the planet in the central 20 AU of the ε Eri system and provide the dynamical information described above with a single observation. The proposed space missions *SPECS* (*Submillimeter Probe of the Evolution of Cosmic Structure*; Leisawitz et al.

1999), Eclipse (Trauger et al. 2003), and the *Darwin* Terrestrial Planet Finder[5] should also be able to make detailed maps of the central dust cloud.

5. CONCLUSIONS

Our simulations suggest that if the inner ring (<20 AU) in the ε Eri debris disk is composed of dust released on low-eccentricity orbits ($e_{dust} \lesssim 0.4$) exterior to the precise-Doppler planet orbiting ε Eri, future submillimeter images of this system should detect an off-center limb-brightened ring and a pair of dust clumps that appear to orbit the star once every 14 yr. If the dust is released on highly eccentric orbits ($e_{dust} \gtrsim 0.4$), we

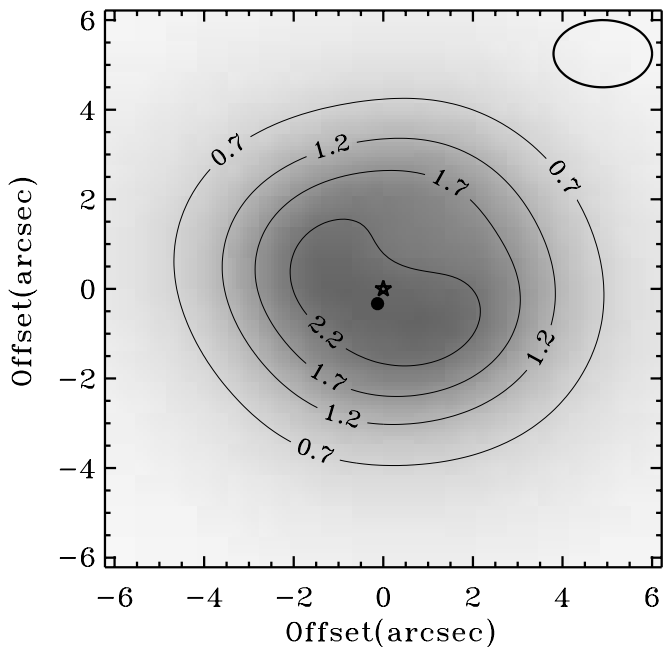[5] See http://planetquest.jpl.nasa.gov.

Fig. 8.—Simulated observations of the comet-dust model by the IRAM PdBI at 1.3 mm. Contours indicate the surface brightness in mJy beam^{-1}.
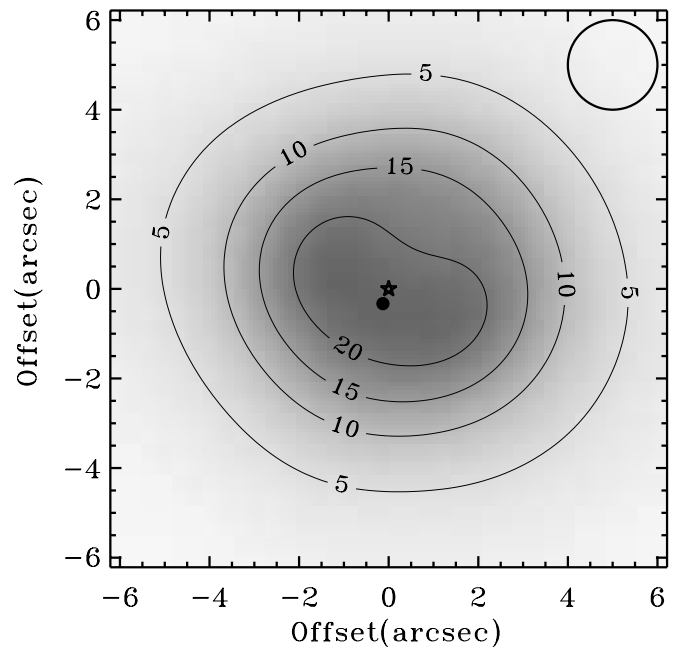

Fig. 9.—Simulated observations of the comet-dust model by the SMA at 450 μm. Contours indicate the surface brightness in mJy beam^{-1}.

would not see rotating dust clumps, but rather an inclined torus of dust with a circular inner void off-center from the star. High-resolution observations of the ϵ Eri dust complex with the IRAM PdBI, the SMA, or ALMA could confirm the existence of the planet reported by Hatzes et al. (2000). Our simulations are not the last word on the structure of this cloud; we do not take into account the mutual collisions of dust grains. However, finding one of the generic structures we predict would constrain the unknown orbital elements of the planet and lend confidence to the practice of interpreting dust-cloud patterns as resonant signatures of extrasolar planets.

REFERENCES

Backman, D. E., & Paresce, F. 1993, in Protostars and Planets III, ed. E. H. Levy & J. I. Lunine (Tucson: Univ. Arizona Press), 1253
Beichman, C. A., Neugebauer, G., Habing, H. J., Clegg, P. E., & Chester, T. J. 1988, IRAS Catalogs and Atlases, Version 2, Explanatory Supplement (NASA Ref. Publ. 1190; Washington: NASA)
Bell, R. A., & Gustafsson, B. 1989, MNRAS, 236, 653
Burns, J. A. 1976, Am. J. Phys. 44, 944
Campbell, B., Walker, G. A. H., & Yang, S. 1988, ApJ, 331, 902
Cumming, A., Marcy, G. W., & Butler, R. P. 1999, ApJ, 526, 890
Danchi, W. C., Deming, D., Kuchner, M. J., & Seager, S. 2003, ApJ, 597, L57
Dent, W. R. F., Walker, H. J., Holland, W. S., & Greaves, J. S. 2000, MNRAS, 314, 702
Dermott, S. F., Jayaraman, S., Xu, Y. L., Gustafson, B. A. S., & Liou, J. C. 1994, Nature, 369, 719
Duncan, M., Quinn, T., & Tremaine, S. 1988, ApJ, 328, L69
Fernandez, J. A. 1980, MNRAS, 192, 481
Gatewood, G. 2000, BAAS, 32, 32.01
Gold, T. 1975, Icarus, 25, 489
Gray, D. F., & Baliunas, S. L. 1995, ApJ, 441, 436
Greaves, J. S., et al. 1998, ApJ, 506, L133
Hatzes, A. P., et al. 2000, ApJ, 544, L145
Holland, W. S., et al. 1998, Nature, 392, 788
———. 2003, ApJ, 582, 1141
Koerner, D. W., Sargent, A. I., & Ostroff, N. A. 2001, ApJ, 560, L181
Kuchner, M. J. 2003, Earth Moon Planets, 92, 435
Kuchner, M. J., & Holman, M. J. 2001, BAAS, 33, 1151
———. 2003, ApJ, 588, 1110
Kuchner, M. J., & Serabyn, E. 2002, ApJ, submitted
Leisawitz, D., Mather, J. C., Moseley, H. S., & Zhang, X. 1999, Ap&SS, 269, 563
Levison, H. F., & Duncan, M. J. 1997, Icarus, 127, 13
Li, A., Lunine, J. I., & Bendo, G. J. 2003, ApJ, 598, L51
Liou, J., & Zook, H. 1999, AJ, 118, 580
Moro-Martín, A., & Malhotra, R. 2003, AJ, 125, 2255
Quillen, A. C., & Thorndike, S. 2002, ApJ, 578, L149
Reach, W. T., et al. 1995, Nature, 374, 521
Robertson, H. P. 1937, MNRAS, 97, 423
Saar, S. H., & Osten, R. A. 1997, MNRAS, 284, 803
Sheret, I., Dent, W. R. F., & Wyatt, M. C. 2004, MNRAS, 348, 1282
Trauger, J. T., et al. 2003, Proc. SPIE, 4854, 116
Wilner, D. J., Holman, M. J., Kuchner, M. J., & Ho, P. T. P. 2002, ApJ, 569, L115
Wisdom, J., & Holman, M. J. 1991, AJ, 102, 1528
Wyatt, S. P., & Whipple, F. L. 1950, ApJ, 111, 134
Zuckerman, B. 2001, ARA&A, 39, 549